Spatial Resolution Requirements for the Application of Temperature and Emissivity Separation (TES) Algorithm Over Urban Areas

Zhijun Zhen, Shengbo Chen, *Member, IEEE*, Tiangang Yin, and Jean-Philippe Gastellu-Etchegorry, *Member, IEEE*

***Abstract*—Current thermal infrared satellite images are full of mixed pixels. This work is a quantitative analysis, based on radiative transfer modelling, of the distribution of mixed pixels and their impact on the use of temperature and emissivity separation (TES). TES was applied to radiance images of the cities of Basel and Heraklion simulated at different spatial resolutions by the DART radiative transfer model with 3-D representations of these cities. The accuracy of the TES was assessed by comparing the retrieved land surface temperature and surface emissivity to the input temperature and emissivity of DART. The spatial resolution of 30 m appeared to be a crucial threshold for the presence of pure pixels in these cities. When the spatial resolution reaches 30 m, the percentage of mixed pixels shows significant growth. We evaluated the performance of the TES algorithm on pure and mixed pixels. For homogeneous, isothermal, flat, and shadowless pure pixels, the variation of TES accuracy with the resolution is not obvious. For mixed pixels or pure pixels with a high nonplanar structure, the accuracy of TES even decreases with the increase of resolution. The reason may be that higher spatial resolution enhances spatial heterogeneity (due to shadow and pixel nonplanarity). A physically acceptable average temperature and average emissivity can be obtained even if TES is applied to mixed pixels. Our study stresses the need to consider the spatial resolution variation effect when applying the TES method to urban areas.**

***Index Terms*—DART, land surface emissivity (LSE), land surface temperature (LST), spatial resolution, temperature and emissivity separation (TES), urban.**

I. Introduction

URBAN temperature, and in particular, the urban heat island, is an essential concern in the context of urban climate change [1], [2], [3], [4]. Accurate retrieval of land surface temperature (LST) and land surface emissivity (LSE) of cities is needed to monitor urban temperatures [5], [6], [7], [8]. LST and spectral LSE can be derived from satellite passive microwave (MW) [9], [10] and thermal infrared (TIR) [11], [12], [13] observations. TIR is more commonly used for urban LST and LSE retrieval [14]. Indeed, although it can overcome cloud cover problems, MW data is low spatial resolution and is more related to subsurface temperature than skin temperature [15], soil humidity and surface roughness [16].

LST and LSE retrieval methods can be categorized according to their calculation techniques: Stepwise and concurrent [14]. Stepwise methods calculate LSE first, then, retrieve LST using the determined LSE. They include the single-channel method [17], the multichannel method [18], and the multiangle method [19]. However, their LST accuracy highly depends on the first retrieved LSE. It underlines the interest in concurrent retrieval of LST and LSE. The temperature and emissivity separation (TES) algorithm [20] and its improvements [21], [22], [23], [24] are among the most used TIR methods for LST and LSE concurrent retrieval [25]. Its performance has been assessed concerning various situations such as surface materials, atmospheric profiles [26], and sky view factor [27] variations influence. However, TES assumes that any pixel is isothermal, pure, and flat [20], which is rarely the case with current TIR satellite image spatial resolutions (i.e., 90 m for advanced spaceborne thermal emission and reflection radiometer (ASTER)) [28]. A few TES-based algorithms, such as thermal remote sensing unmixing for subpixel temperature (TRUST) [22] and TRUST-day and night synergy (TRUST-DNS) [23], consider nonisothermal mixed pixels. However, they are significantly influenced by spatial resolution [22], [23].

Although the spatial resolution impacts TES results due to spectral confusion and the difficulty of getting high-resolution TIR images, its effect has not been extensively studied, especially in urban areas where significant heterogeneity exists. Radiative transfer models combined with 3-D representations of cities are potential tools to quantify this effect, provided they efficiently simulate TIR images at any spatial resolution and inform on each pixel's components and temperature/optical properties [29]. Here, we use the DART model [30], [31], [32], [33], [34], [35], [36]. This 3-D radiative transfer model has already been validated in the visible and thermal infrared domains

Manuscript received 24 April 2022; revised 10 July 2022; accepted 20 September 2022. Date of publication 4 October 2022; date of current version 24 October 2022. This work was supported in part by the National Natural Science Foundation of China (NSFC) under Grant 42201372, in part by the TOSCA program of the French space center (CNES), and in part by China Scholarship Council (CSC). *(Corresponding authors: Jean-Philippe Gastellu-Etchegorry; Shengbo Chen.)*

Zhijun Zhen is with the College of Geoexploration Science and Technology, Jilin University, Changchun 130026, China, and also with the Centre d'Etudes Spatiales de la Biosphere (CESBIO), University of Toulouse, 31401 Toulouse, France (e-mail: zhenzj18@mails.jlu.edu.cn).

Shengbo Chen is with the College of Geoexploration Science and Technology, Jilin University, Changchun 130026, China (e-mail: chensb@jlu.edu.cn).

Tiangang Yin is with the Land Surveying and Geo-Informatics, The Hong Kong Polytechnic University, Hong Kong, SAR, China (e-mail: tiangang.yin.85@gmail.com).

Jean-Philippe Gastellu-Etchegorry is with the Centre d'Etudes Spatiales de la Biosphere (CESBIO), University of Toulouse, 31401 Toulouse, France (e-mail: jean-philippe.gastellu-etchegorry@cesbio.cnes.fr).

Digital Object Identifier 10.1109/JSTARS.2022.3211502

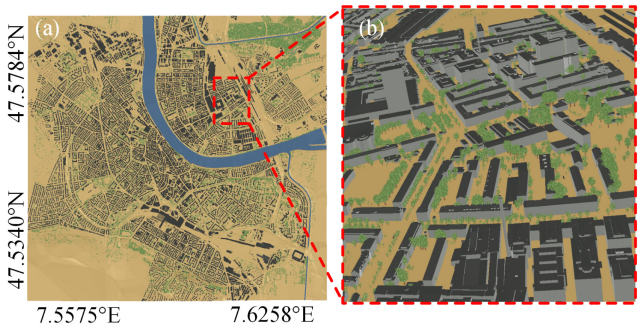

Fig. 1. Basel 3-D urban geometric database. (a) Top view. (b) Side view of the red square in (a). Buildings (roofs: Dark, walls: Light grey), trees (green), water (blue), and ground (yellow).

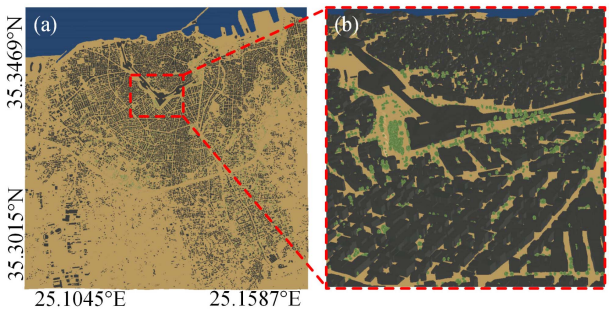

Fig. 2. Heraklion 3-D urban geometric database. (a) Top view. (b) Side view of the red square in (a). Trees (green), ground (yellow), buildings (walls and roofs: Gray), and water (blue).

[37], [38], [39]. Its wide range of applications includes look-up tables creation for the inversion of remote sensing images [40], [41], [42], and validation works [43], [44], [45].

This work assessed the spatial resolution requirements for the TES method in urban areas. We used 3-D urban structure databases of the cities of Basel and Heraklion, and DART simulated bottom of the atmosphere (BOA) radiance images to identify the distribution of pure and mixed pixels over the study areas for various spatial resolutions. The TES method was applied to the DART images to retrieve LST and LSE, whose accuracy was assessed by comparing them to the emissivity and temperature input into DART.

II. Study Areas and Methods

A. Study Areas

The studied cities, Basel and Heraklion, were research targets of the urban anthropogenic heat flux from the earth observation satellites (URBANFLUXES) [46] project. Basel is on the river Rhine in northwestern Switzerland, where the Swiss, French, and German borders meet [47], [48]. Our study area encompasses it almost completely (latitude from 47.5340°N to 47.5784°N, and longitude from 7.5575°E to 7.6258°E). Its geometric database is very detailed (Fig. 1). Heraklion is the largest city in Crete, Greece. It is a rapidly growing urban area with a mixed land utilization pattern, including residential, commercial, industrial, and rural [49]. Our study area contains the center of Heraklion (latitude from 35.3015°N to 35.3469°N, longitude from 25.1045°E to 25.1587°E). Heraklion has a much less detailed geometric database (Fig. 2) than Basel (e.g., all roofs are horizontal). These two cities are characteristic European cities: Basel is a typical inland European city, and Heraklion is a common Mediterranean coastal city. Therefore, our results can be extended to other European cities.

The city 3-D mock-ups were initially prepared and used by Landier et al. [47], [48], [50]. The land cover classes of Basel and Heraklion include buildings, impervious, water, low vegetation, bare soil, deciduous, and evergreen, according to the URBANFLUXES project [51], [52]. We grouped some classes: The tree class contains deciduous and evergreen vegetation; the ground class contains impervious surface, low vegetation, and bare soils; and the building and water classes are the same as in the URBANFLUXES project. Here, water is considered the opaque plane. All urban components' location and geometric structure, including the local digital elevation model, are from the local urban databases. Tree location, height, and crown dimensions are from field measurements. In DART, we simulated trunks as regular octahedrons and crowns as ellipsoidal volumes homogeneously filled with small triangles in order to mimic the so-called turbid medium (i.e., infinite number of infinitely small facets with a statistical angular orientation) commonly used in modelling works for remote sensing studies. More detailed information on the city databases can be found in the literature [47].

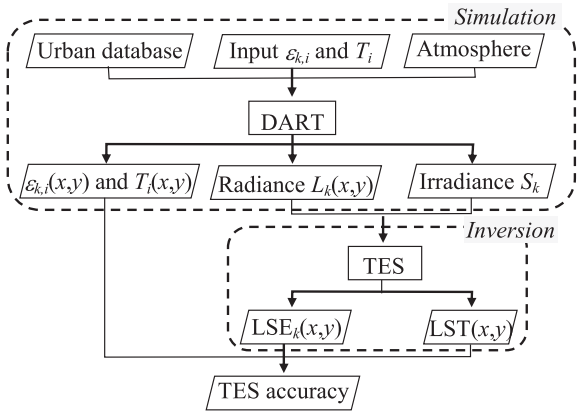

Fig. 3. Flowdiagram of our procedure. DART simulates BOA irradiance S_k and radiance $L_k(x,y)$ images per pixel (x,y) for band k using temperature T_i and emissivity $\varepsilon_{k,i}$ per scene component i. Then, TES computes $LST(x,y)$ and $LSE_k(x,y)$ using S_k and $L_k(x,y)$.

B. Methods

Fig. 3 shows the flow diagram of our procedure for studying the influence of spatial resolution on the TES method. First, for each city, DART simulated the BOA irradiance S_k and the upwelling radiance $L_k(x,y)$ image using its geometric urban database and gave 3-D distributions of optical properties and temperature values in the urban scene and atmosphere. Then, TES derived the urban LSE and LST from the BOA irradiance and upwelling radiance images. Finally, the retrieved urban LSE

and LST were compared to those used as DART input parameters to assess the TES algorithm's accuracy.

1) DART Model: DART (https://dart.omp.eu) is a 3-D radiative transfer model that has been developing since 1992 at CESBIO, Toulouse, France, and patented in 2003. Its licenses are free for research. It simulates remote sensing images and the radiative budget of urban and natural landscapes from the visible to thermal infrared domains. It has already been validated by various works [53].

Here, DART was run with gas and aerosol models [54], which were already used [47] to compute the time series of radiative budget maps of Basel and Heraklion (Table III). We investigated TES accuracy of did not study the influence of the atmosphere on TES accuracy because it was studied before [27]. By importing urban geometric databases, DART created urban mock-ups with four urban components (i.e., trees, buildings, water, ground) made up of small facets, each with constant optical properties from the ASTER or DART spectral library, and resample them to the ASTER wavelength using the ASTER spectral response function [55]. A typical class was chosen for each land cover, and the median value of all spectral curves under that class was taken as input. The roof, ground, and water emissivities were selected from the ASTER spectral library. The general construction materials class was selected as buildings optical property input, the spodosol class was selected as ground optical property input, and the water class was selected as water optical property input. The tree spectral was a little special because the ASTER spectral library only provided hemispherical reflectance for vegetation. However, the DART model required inputting the leaf reflectance and transmittance. Therefore, the vegetation input optical properties were selected as the median value of all vegetation spectral with reflectance and transmittance value in the DART database and resampled to the ASTER wavelength using the ASTER spectral response function.

We used the mean and delta value to describe the component temperature for considering the difference between sunlit and shaded parts. The mean and delta temperature values were derived from the literature [7], [56]. DART can calculate the temperature of each facet based on the mean and delta temperature, and these values were used to validate the accuracy of the TES method. Therefore, even the same type of land cover had different temperatures. The solar direction was selected as the sun's position on February 29, 2020, at 10:30 A.M. (local time). This date was selected because the temperature values were measured on that day, and the time was selected because it corresponded to the common time of ASTER passing territory (https://asterweb.jpl.nasa.gov/).

DART simulated BOA irradiance S_k and nadir (i.e., view zenith angle (VZA) equal 0°) radiance L_k images of the cities at nine satellite spatial resolutions (5 m, 10 m, 30 m, 50 m, 70 m, 90 m, 120 m, 300 m, and 1000 m) for each band k of the five ASTER TIR bands (Table III). It also simulated a spectral nadir component radiance image per urban component (e.g., ground). A great feature of component images was to inform the distribution of the mixed pixels.

2) TES Method: The TES method used DART simulated BOA TIR radiance $L_k(x,y)$ and atmosphere downwelling irradiance S_k images to derive $\mathrm{LSE}_k(x,y)$ images per band k and a $\mathrm{LST}(x,y)$ image. Three successive modules iteratively processed all pixels of the L_k and S_k images: normalized emissivity method (NEM) module [57], ratio algorithm (RAT) module [58], and maximum–minimum apparent emissivity difference (MMD) module [59]. They are briefly presented below. Detailed information is given by Gillespie et al. [20].

- *NEM module*. It iteratively refines the temperature T_{NEM} and emissivity $\varepsilon_{\mathrm{NEM},k}$ that it links with

$$L_k = \varepsilon_{\mathrm{NEM},k} \cdot B_k\left(T_{\mathrm{NEM}}\right) + \left(1 - \varepsilon_{\mathrm{NEM},k}\right) \cdot \frac{S_k}{\pi} \tag{1}$$

with $B_k(T_{\mathrm{NEM}})$ the Planck's law and $\varepsilon_{\mathrm{NEM},k}$ the emissivity for band k. The first term of (1) is the radiance R_k emitted by the land surface, and the second term is the downwelling atmospheric radiance reflected by the land surface. Two expressions are used to represent R_k

$$R_k = L_k - \left(1 - \varepsilon_{\mathrm{NEM},k}\right) \cdot \frac{S_k}{\pi} \tag{2}$$

$$R_k = \varepsilon_{\mathrm{NEM},k} \cdot B_k\left(T_{\mathrm{NEM}}\right). \tag{3}$$

First, iteration 0 computes R_k^0 with (2) and a maximum initial $\varepsilon_{\mathrm{NEM},k}^0$, usually 0.99. Then, $\varepsilon_{\mathrm{NEM},k}^0$ is refined [60]: T_k^0 is derived from $\varepsilon_{\mathrm{NEM},k}^0$ and R_k^0 by applying the inverse Planck's law to (3) for each band k, and the highest T_k^0 value is chosen as T_{NEM}^0. Then, (3) gives $\varepsilon_{\mathrm{NEM},k}^1$, using T_{NEM}^0 and R_k^0. In iteration 1, (2) gives R_k^1 using $\varepsilon_{\mathrm{NEM},k}^1$. Then, T_{NEM}^1 is derived from R_k^1 using (3), and so on. The iterative process ends if the difference of R_k from two consecutive iterations is smaller than a given threshold or if the number of iterations reaches a maximum value (usually 12) [60]. The threshold can be the radiance equivalent to the noise equivalent temperature difference of the sensor [60] (i.e., 300±0.3 K for the ASTER sensor [20]). Then, a long procedure [60] is checked to see if the $\varepsilon_{\mathrm{NEM},k}^0 = 0.99$ value can be refined or not. If it can be refined, then a new initial $\varepsilon_{\mathrm{NEM},k}^0$ is used to compute R_k^0 with (2) and restart the iterative processes (see [60] for details). If it cannot be refined, then the existing $\varepsilon_{\mathrm{NEM},k}$ values are further refined by the RAT and MMD modules.

- *RAT module*. It computes spectral indices β_k that do not depend on temperature because ratios of spectral radiances are assumed to be nearly independent of temperature

$$\beta_k = \frac{\varepsilon_{\mathrm{NEM},k}}{\bar{\varepsilon}} \tag{4}$$

with $\bar{\varepsilon}$ the mean value of $\varepsilon_{\mathrm{NEM},k}$ over all k bands. Then, the MMD module must scale β_k to the actual emissivity values.

- *MMD module*. First, it computes the range MMD of β_k values

$$\mathrm{MMD} = \max\left(\beta_k\right) - \min\left(\beta_k\right). \tag{5}$$

Then, $\varepsilon_{\min}$ is computed as

$$\varepsilon_{\min} = \begin{cases} a - b * \mathrm{MMD}^c & (\mathrm{MMD} \geq 0.03) \\ 0.983 & (\mathrm{MMD} < 0.03) \end{cases} \tag{6}$$

TABLE I
REGRESSION COEFFICIENTS AND DETERMINATION R^2 OF MMD MODULE

Sensors	Coefficients			R^2
	a	b	c	
ASTER	0.994	−0.687	0.737	0.983
TASI*	1.001	−0.737	0.760	0.997
AHS**	1.000	−0.782	0.817	0.994

* TASI: Thermal Airborne hyper Spectral Imager.
** AHS: Airborne Hyperspectral Scanner sensor.

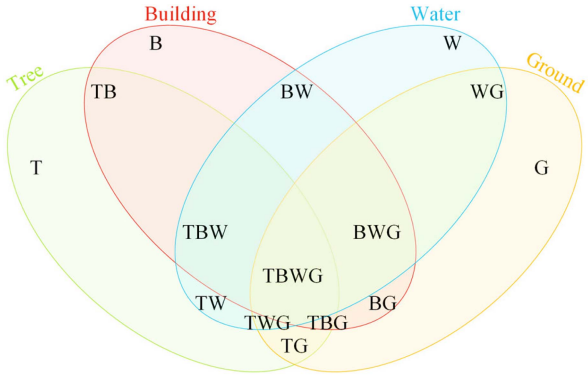

Fig. 4. Pixel type abbreviations: The first letter presents the component for pure pixels, and a combination of the first letters presents components for mixed pixels.

with a, b, and c as sensor-dependent regression coefficients. Table I lists the MMD coefficients of three sensors [21], [22]. We chose ASTER coefficients because we used the TIR bands of the ASTER.

The TES-derived emissivity $\varepsilon_{\mathrm{TES},k}$ is computed as:

$$\varepsilon_{\mathrm{TES},k} = \beta_k \cdot \left(\frac{\varepsilon_{\min}}{\min(\beta_k)} \right). \tag{7}$$

Then, the TES-derived surface temperature T_{TES} is computed by applying the inverse Planck's law in (3) using R_k computed in (2) with the maximum value of $\varepsilon_{\mathrm{TES},k}$. Conversely to the ASTER method [20], we did not use a final correction for sky irradiance because the following versions reported that this correction is limited and influenced by atmospheric correction errors [60].

III. MIXED PIXEL DISTRIBUTION AND TES ACCURACY ASSESSMENT

A. Mixed Pixel Distribution With Spatial Resolutions

We used the DART simulated component images to study the mixed pixel effect in urban sites. For simplicity, we used abbreviated letters to represent a specific pixel type. Fig. 4 details the abbreviation rules, and Fig. 5 shows the distribution of components in mixed pixels in the scene as spatial resolution functions. The total number of pixels for nine spatial resolutions is shown in Table II. The analysis was done from 3 aspects: component percentage variations, percentage variation of mixed pixels, and pure pixel variation rate with spatial resolutions.

1) Component Percentage Variation: The spatial resolution significantly influenced the percentage of pixels per component

TABLE II
TOTAL NUMBER OF PIXELS FOR NINE SPATIAL RESOLUTIONS IN TWO STUDY AREAS

Spatial resolution (m)	Cities	
	Basel	Heraklion
5	1070600	1000000
10	267650	250000
30	30082	27889
50	10706	10000
70	5548	5256
90	3420	3192
120	1935	1764
300	324	289
1000	36	25

(Fig. 5). For example, the percentage of pixels that contain ground was 82.76% for Basel and 79.22% for Heraklion at 5-m resolution; at 1000-m resolution, it increased up to 100.00% for Basel and 100.00% for Heraklion. Pixels with water were a small category. At 5-m resolution, their percentage was 4.89% for Basel and 9.90% for Heraklion; at 1000-m resolution, it increased up to 44.44% for Basel and 28.00% for Heraklion. The spatial resolution affected the mixed pixel distribution of trees and buildings more than that of ground and water. For example, at 5-m resolution, the percentage of pixels with buildings was 31.75% for Basel and 32.58% for Heraklion; at 1000-m resolution, it increased up to 91.67% in Basel and 100.00% in Heraklion. From 5 m- to 1000-m resolution, the percentage of pixels with trees increased from 25.73% to 97.22% in Basel and from 7.34% to 84.00% in Heraklion. These significant increases could be due to trees and buildings being small size components distributed over the whole urban area. Therefore, with spatial resolution coarsening, the percentage of pixels containing trees and buildings increased faster than ground and water.

2) Percentage Variation of Mixed Pixels: The spatial resolution also influenced the spatial distribution of pure and mixed pixels (Fig. 5). As expected, the percentage of pure pixels significantly decreased with the coarsening of spatial resolution (Table IV). At 5-m resolution, it was 59.66% in Basel and 72.94% in Heraklion. At 1000-m resolution, it dramatically decreased to 2.78% in Basel and 0.00% in Heraklion. From 5-m resolution to 1000-m resolution, the percentages of pixels with two components decreased from 35.53% to 5.56% in Basel, and from 25.09% to 12.00% in Heraklion. The total percentages of three-component pixels increased with spatial resolution coarsening, from 4.80% (Basel) and 1.98% (Heraklion) at 5-m resolution to 47.22% (Basel) and 64.00% (Heraklion) at 1000-m resolution in Basel. Four-component pixels appeared at 5-m resolution in Basel with 0.01% and at 30-m resolution in Heraklion with 0.01%; at 1000-m resolution, these percentages increased to 44.44% in Basel and 24.00% in Heraklion.

Depending on the study city, there were also variations in the mixed pixels components' proportions. In Basel city, the largest proportion of combinations for the two-component pixels was the TG pixels (18.34% at 5-m resolution and 5.56% at 1000

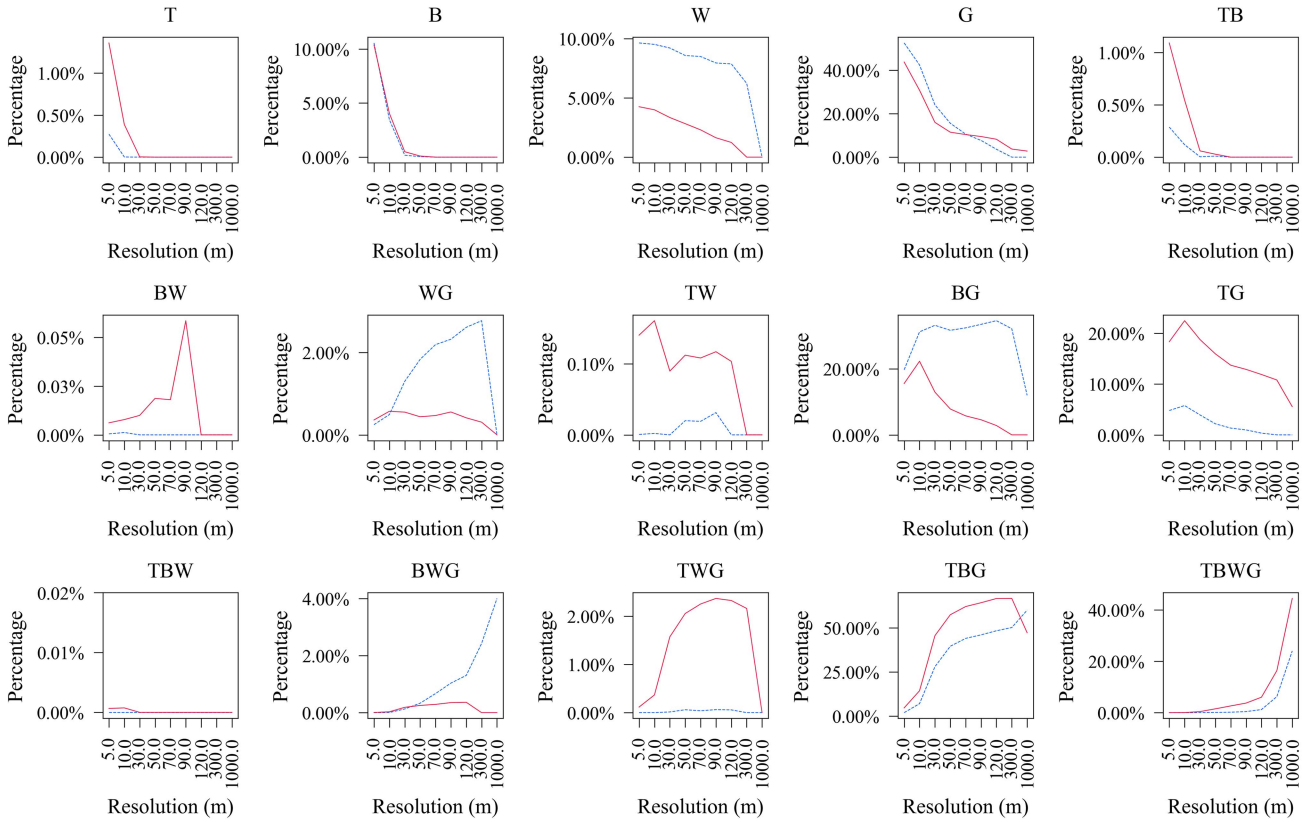

Fig. 5. Proportion of the pixels types as a function of the spatial resolution for Heraklion and Basel. Fig. 4 gives the meaning of the abbreviated titles. The *x*-axis is nonlinear.

TABLE III
INPUT DART PARAMETERS FOR THE IMAGE SIMULATIONS

Components	T_i **(mean, delta)**	$\varepsilon_{k,i}$ 8.3μm	8.65μm	9.1μm	10.6μm	11.3μm
Trees	305.65, 6.00	0.9726	0.9656	0.9573	0.9597	0.9628
Buildings	304.90, 4.50	0.9545	0.9511	0.9455	0.9305	0.9307
Water	302.42, 0.00	0.9830	0.9838	0.9850	0.9906	0.9904
Ground	311.65, 17.00	0.9828	0.9822	0.9781	0.9703	0.9669
Cities	**VZA(°)**	**VAA(°)**		**SZA(°)**		**SAA(°)**
Basel	0	0		62.5		217.5
Heraklion	0	0		60.7		234.1
- Gas model: USSTD76 - **Aerosol model:** USSTD76 RURALV23						
- Spatial resolution: 5 m, 10 m, 30 m, 50 m, 70 m, 90 m, 120 m, 300 m, 1000 m						

Note: sun zenith and azimuth angle are set to the sun location of the corresponding city on February 29 2020, at 10:30 A.M. at the local time.

m), followed by the BG pixels (15.59% at 5-m resolution and 0.00% at 1000 m). The largest proportion of the combination was the TBG pixels for the three-component pixels (1.98% at 5-m resolution and 60.00% at 1000 m). In addition, there were nearly no TBW pixels. BG was the most extensive combination of the two-component pixels in Heraklion city (19.75% at 5-m resolution and 12.00% at 1000 m). TBG was the largest proportion of the combination for the three-component pixels (1.98% at 5-m resolution and 60.00% at 1000 m). There were nearly no T, BW, TW, and TBW pixels.

3) Pure Pixel Variation Rate With Spatial Resolution: With the image spatial resolution getting coarse, there was a significant decrease in the proportion of pure pixels. Both two-component and three-component pixels show a trend of increasing first and then decreasing. The proportion of four-component pixels increases with spatial resolutions.

The decrease in pure pixels shows a nonlinear relationship with the decrease in spatial resolution (Fig. 5), with the threshold at the 30-m spatial resolution. When the spatial resolution is below 30 m, the proportion of pure pixels increases slowly

TABLE IV
PERCENTAGE OF PURE PIXELS AT NINE SPATIAL RESOLUTIONS

Spatial resolution (m)	Cities	
	Basel	Heraklion
5	59.66%	72.94%
10	39.14%	55.31%
30	19.82%	33.39%
50	14.39%	24.20%
70	12.69%	19.10%
90	11.11%	15.63%
120	9.46%	11.51%
300	3.70%	6.23%
1000	2.78%	0.00%

with increasing spatial resolution. However, when the spatial resolution is higher than 30 m, the proportion of pure pixels increases rapidly with increasing spatial resolution. Therefore, 30 m can be considered a critical resolution threshold for some algorithms that assume enough pure pixels in the images (i.e., TES) over the urban area. For spatial resolution decrease from 5 m to 30 m, pure building pixel decreased from 10.37% to 0.50% in Basel and from 10.56% to 0.18% in Heraklion; pure ground pixel decreased from 43.67% to 15.97% in Basel and from 52.45% to 23.99% in Heraklion; pure water pixel decreased from 4.26% to 3.34% in Basel and from 9.65% to 9.22% in Heraklion. Water and ground had a relatively less distinct variation in spatial resolution due to their high spatial continuity. All pure pixels are no longer present, except for the ground pure pixels in Basel (2.78%) at the spatial resolution of 1000 m.

B. TES Accuracy With Varying Sensor Spatial Resolutions

The performance of TES for pure and mixed pixels was assessed using DART simulated L_k and S_k as input data of TES. In this section, first, we defined the acceptable pixel of TES of this article. Then, we studied the retrieved LSE and LST distribution from TES. Finally, a detailed accuracy assessment was carried out for TES performance evaluation.

1) Definition of the Acceptable Pixels: We use the definition of r-emissivity (independent of temperature) [61], [62] as the mixed pixel emissivity, and then the temperature derived using the TES method from the mixed pixels can be considered the equivalent average temperature. Determining the true LST value of the mixed pixel is complex. We take an example of a flat and nonisothermal mixed pixel comprised of two components. Then, the radiance R_k emitted by the mixed pixel at band k is [63]

$$\begin{aligned} R_k &= a_1\varepsilon_{1,k}B_k\left(T_1\right) + a_2\varepsilon_{2,k}B_k\left(T_2\right) \\ &= \left(a_1\varepsilon_{1,k} + a_2\varepsilon_{2,k}\right)B_k\left(\bar{T}\right) \end{aligned} \tag{8}$$

where a_1 and a_2 are the area ratio for each component, $\varepsilon_{1,k}$, $\varepsilon_{2,k}$ and T_1, T_2 are the r-emissivity and temperature for each component, and B_k is the Planck function. By using the Taylor expansion on (8) at T_1 and T_2, and omitting second-order and higher-order terms, we can get

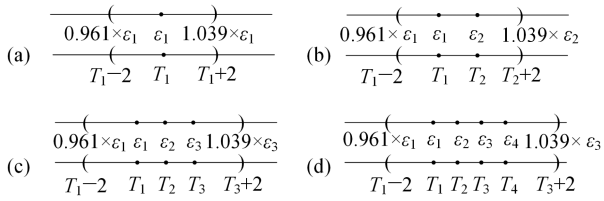

Fig. 6. Example of tolerant boundaries for the TES inversion. Case $\varepsilon_1<\varepsilon_2<\varepsilon_3<\varepsilon_4$ and $T_1<T_2<T_3<T_4$, where the tolerant boundary depends on the minimum and maximum values of the pixel components. (a) Pure pixel. (b) Two-component pixel. (c) Three-component pixel. (d) Four-component pixel. $\varepsilon_{k,i}$ and T_i are DART input emissivity and temperature of component i, respectively.

$$B_k\left(\bar{T}\right) = B_k\left(T_1\right) + \frac{a_2\varepsilon_{2,k}\frac{\partial B}{\partial T}\big|_{T=T_1}\left(T_2-T_1\right)}{a_1\varepsilon_{1,k}+a_2\varepsilon_{2,k}} \tag{9}$$

$$B_k\left(\bar{T}\right) = B_k\left(T_2\right) - \frac{a_1\varepsilon_{1,k}\frac{\partial B}{\partial T}\big|_{T=T_2}\left(T_2-T_1\right)}{a_1\varepsilon_{1,k}+a_2\varepsilon_{2,k}}\ . \tag{10}$$

Based on (9) and (10), the equivalent average temperature $\bar{T}$ should be between T_1 and T_2, and is a function of component area ratio, emissivity and temperature difference. Therefore, we assumed that the retrieved LSE and LST should lie within the maximum and minimum range of the endmembers involved in the mixing and an acceptable pixel as a pixel with a TES retrieved value LST or LSE within the maximum and minimum value plus the tolerance boundary. The tolerance boundary was set as $\pm 3.9\%$ for emissivity and ± 2K for temperature, according to Carrió et al. [64], who used high-resolution airborne images and in situ data to evaluate TES accuracy on pure pixels over the urban areas, which is consistent to our study target. Because the tolerance boundary increased with the increase of components in a single pixel, a pixel was marked as acceptable if its emissivity in all bands and its temperature were all in the acceptable boundary. This definition aimed to give the number of pixels producing problematic values and not quantify the accuracy of the mixing emissivity and temperature obtained by the TES algorithm. The statistical number of acceptable pixels was employed to quantify the TES accuracy (Fig. 6). Indeed, this acceptable boundary is a rough criterion for evaluating the accuracy of the TES.

2) Retrieved LSE and LST: Figs. 7 and 8 show the retrieved LSE and LST for Basel, respectively. Similarly, Figs. 9 and 10 show the retrieved LSE and LST for Heraklion, respectively. Generally speaking, whether pure or mixed pixel, the value range of LST and LSE from the TES inversion becomes wide as the spatial resolution increases. We examined the simulated images and found that this was due to the wide value range for the pixel radiance in the high spatial resolution images because of heterogeneity (i.e., shadow and pixel nonplanarity). Water is a special case, and the retrieved LST and LSE of water nearly do not vary with spatial resolutions because, in our simulation, it is set very homogeneous (flat and isothermal, with nearly no shadows on it). The retrieved temperatures of trees show a dramatic difference between Basel and Heraklion. The reason for

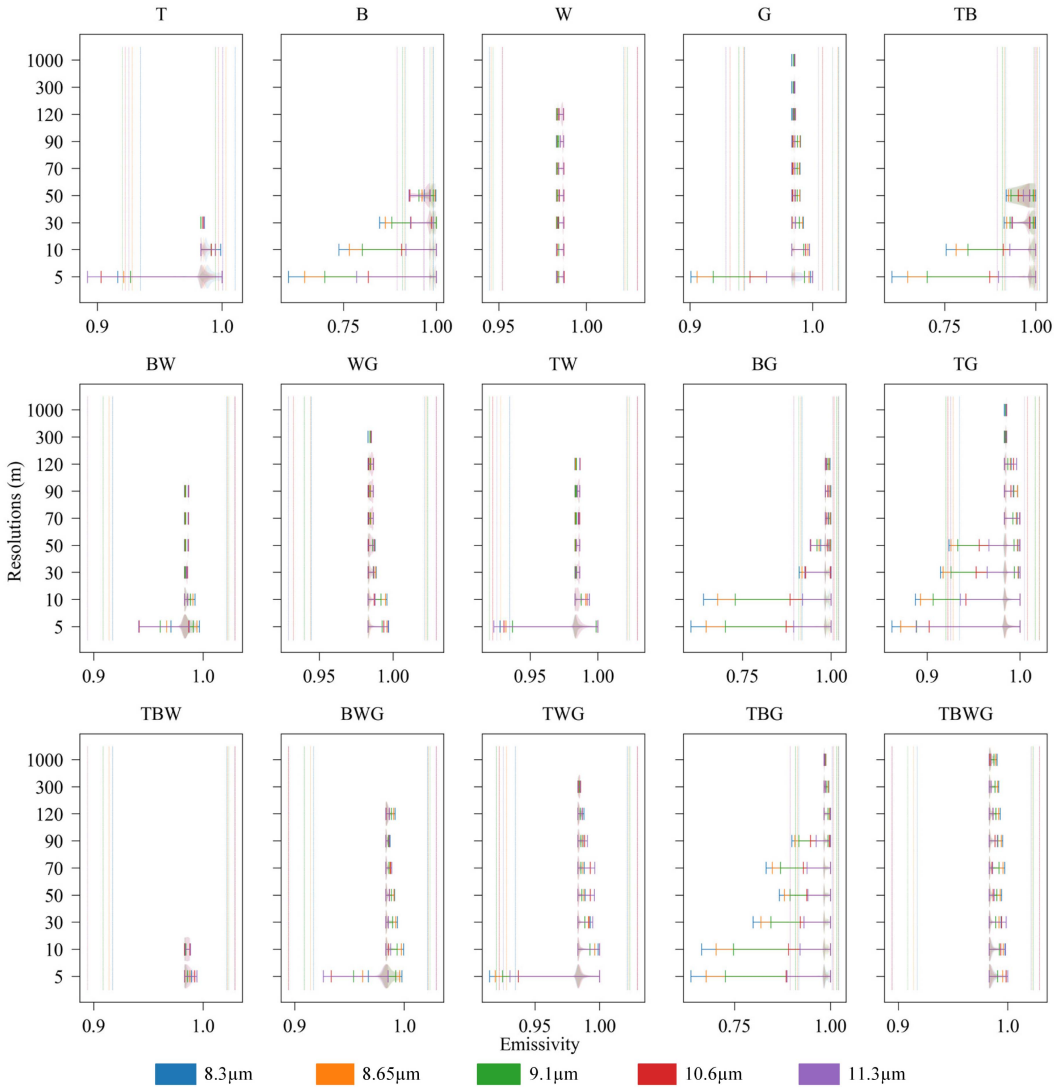

Fig. 7. TES retrieved pixelwise land surface emissivity for Basel at nine spatial resolutions. The vertical dashed lines present the acceptable boundaries for each band. All subplots share the *y*-axis. The spatial resolutions with no violin indicate no corresponding pixels type at that spatial resolution. See Fig. 4 for the meaning of the abbreviated titles of subplots.

this may be due to the distribution pattern in each city. In Basel, trees are concentrated northeast of the city and form a small forest. However, in Heraklion, trees are scattered throughout the interior of the city.

3) Accuracy Assessment: To quantitatively evaluate the percentage of acceptable pixels in the images at the nine spatial resolutions, we considered the ratio $\mathcal{P}$ to equal the "total number of acceptable pixels divided by the total number of pixels" (Table V). The percentage of acceptable pixels increased with spatial resolution coarsening. For example, at 1000-m resolution, nearly all the pixels are within the acceptable boundary in both Basel and Heraklion. Therefore, even for mixed pixels, the TES algorithm can retrieve acceptable average emissivity and average temperature. However, this value is only 89.02% in Basel and 79.18% in Heraklion at 5-m resolution. Reasons for this may be two: First, the acceptable boundary increase with the number of components in the pixel. Second, when the resolution becomes high, the range of LST and LSE obtained by TES become wide due to the enhancement of land cover heterogeneity.

TABLE V
RATIO $\mathcal{P}$ (TOTAL NUMBER OF ACCEPTABLE PIXELS DIVIDED BY THE TOTAL NUMBER OF PIXELS) AT NINE SPATIAL RESOLUTIONS

Spatial resolution (m)	Cities	
	Basel	Heraklion
5	89.02%	79.18%
10	95.75%	89.79%
30	99.32%	96.91%
50	99.77%	98.71%
70	99.95%	99.56%
90	99.88%	99.91%
120	100.00%	99.94%
300	100.00%	100.00%
1000	100.00%	100.00%

The better performance of Basel over Heraklion can be explained by the low performance of trees in both pure and mixed

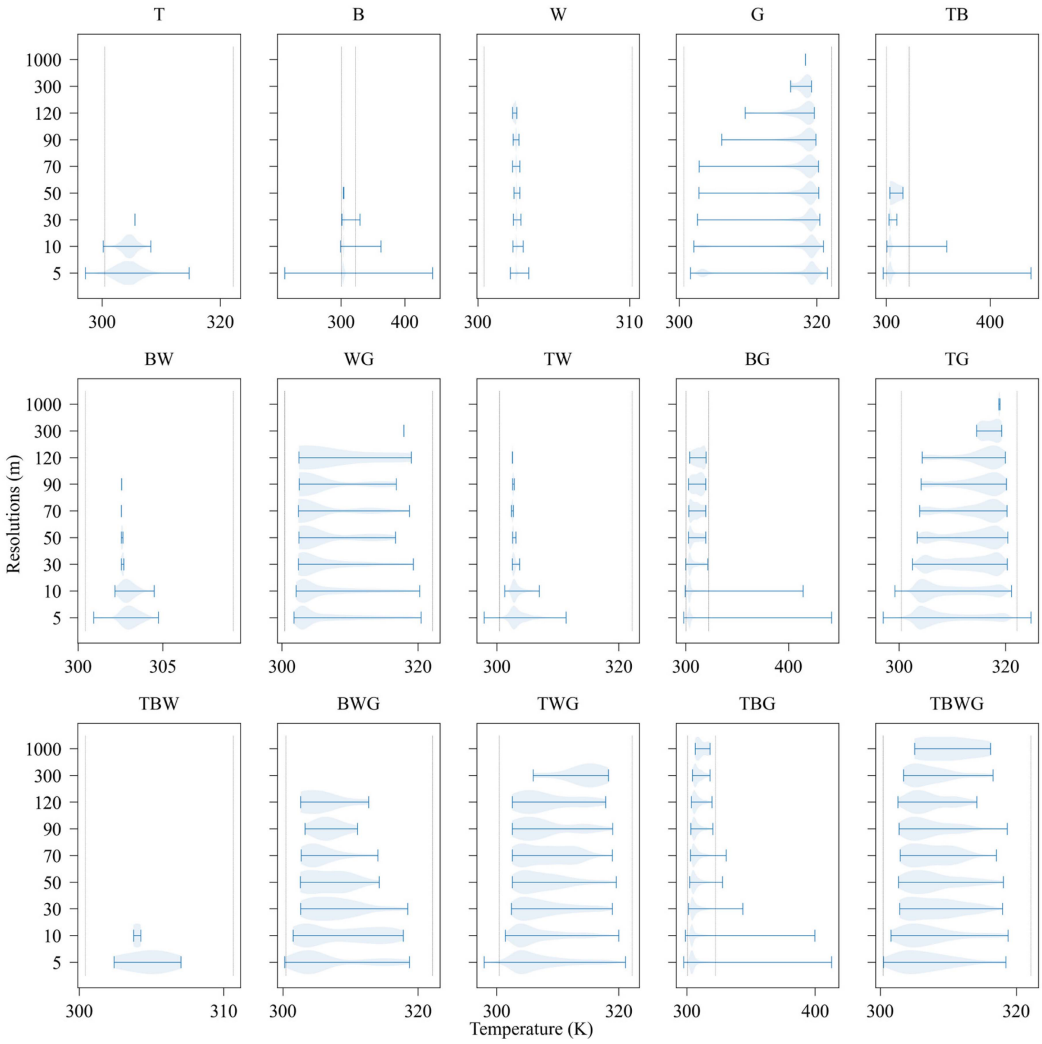

Fig. 8. TES retrieved pixelwise land surface temperatures for Basel at nine spatial resolutions. The two vertical black dashed lines show the most tolerant acceptable boundary. (Because shadows can lead to changes in temperature, the acceptable boundaries are different even for the same pixel type. So here we drew the longest boundary of each type of pixel.) All subplots share the *y*-axis. See Fig. 4 for the meaning of the abbreviated titles of subplots. The spatial resolutions with no violin indicate no corresponding pixels type at that spatial resolution.

pixels because trees are more scattered in Heraklion than in Basel (Fig. 11). The buildings show a slightly different performance between Basel and Heraklion. The accuracy of the roof in Basel seems to slightly decrease with the resolution, while the accuracy of the roof in Heraklion seems to slightly increase with the resolution. Fig. 5 shows that the percentage of pure roof pixels in Basel and Heraklion are almost identical. The main difference between the Basel and Heraklion is the roofs being flat in the mock-up of Heraklion, while its 3-D structure is very detailed in Basel. Therefore, we guess the accuracy of pure flat pixel increases slightly with resolution, while the accuracy of pure nonflat pixel decreases slightly with resolution. The reason for this may be due to the error induced by the 3-D structure of an urban canyon [27].

The performance was poor for pure tree and building pixels. Many works [65], [66], [67] have reported the low performance of vegetation due to the low emissivity spectral contrast. The building's low performance can be due to the relatively large MMD module error [26]. Besides, trees and buildings have relatively small individual geometry sizes, making it much easier to be influenced by their surrounding pixels. The mixed pixel types containing trees or buildings (i.e., TB, TW, TG, TBG) may also show low performance compared to others.

IV. Discussion and Conclusion

A. Discussion

1) Mixed Pixel Distributions: The sensor's spatial resolution is critical for urban studies due to the high heterogeneity within urban areas [68]. Various spatial resolution thresholds have been proposed for urban studies depending on the objectives of the studies. For example, Zhang et al. [69] suggested that 30 m is a too coarse spatial resolution (i.e., Landsat) for urban land use and land cover studies based on visual interpretation due to the widely existing mixed pixels effect. Our study confirms this finding. Indeed, only 19.82% (Basel) and 33.39% (Heraklion) of

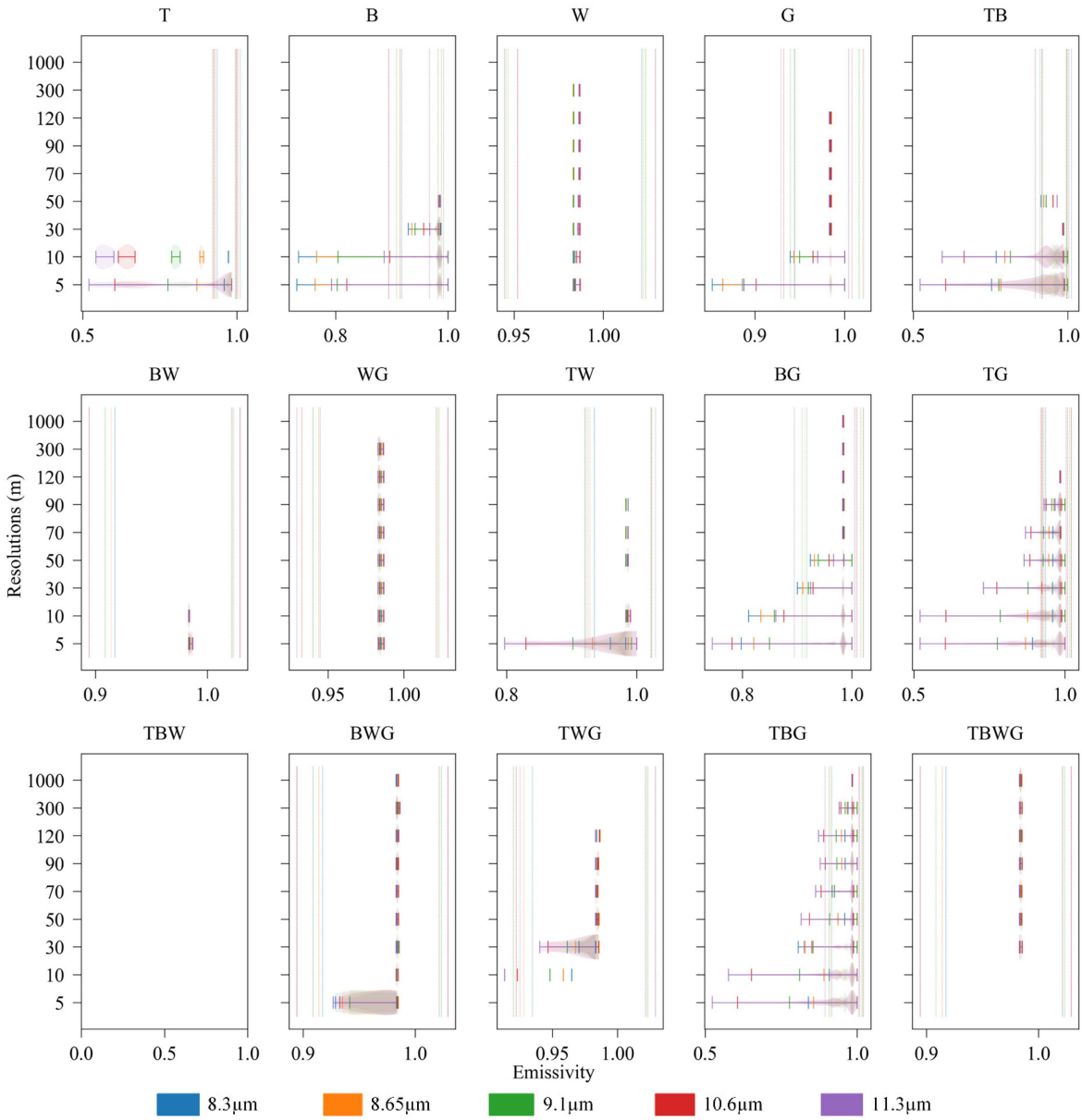

Fig. 9. TES retrieved pixelwise land surface emissivity for Heraklion at nine spatial resolutions. The vertical dashed lines present the acceptable boundaries for each band. All subplots share the *y*-axis. See Fig. 4 for the meaning of the abbreviated titles of subplots. The spatial resolutions with no violin indicate no corresponding pixels type at that spatial resolution.

pixels are pure in the 30-m resolution image. Similarly, Sobrino et al. [70] found that spatial resolution higher than 50 m is needed to evaluate the urban heat island effect properly. In our study, only 14.39% (Basel) and 24.20% (Heraklion) are pure pixels at 50-m resolution, suggesting that the 50 m resolution smooths out the component temperature. Welch [28] demonstrated that a 0.5–10 m spatial resolution is needed to capture the high frequency, low-contrast features of cities.

The fact that the number of pure building pixels greatly decreases when the satellite spatial resolution changes from 5 m to 30 m is also consistent with the common dimensions of urban elements. For example, the width of streets and buildings in downtown Nuremberg, Germany, is around 15 m [71]. Our study stresses that the spatial resolution of the sensor strongly influences the proportion of pure pixels of buildings and trees in the city. It is related to urban design. Indeed, due to lighting requirements, buildings tend to be distributed in a discrete linear pattern so that the relative size of the width of buildings and the sensor spatial resolution directly determine the percentage of pure building pixels in images. A similar rule applies to trees that also appear as lines on both sides of streets.

2) TES Accuracy: TES assumes that pixels are pure, isothermal, and flat, but the percentage of pure pixels in urban areas greatly depends on the sensor spatial resolution, with 30 m being a critical range, as shown by our work. The resolution of remote sensing images should not be less than 30 m in order to obtain LSE and LST of pure pixels. However, few thermal infrared satellite sensors are currently available at this resolution

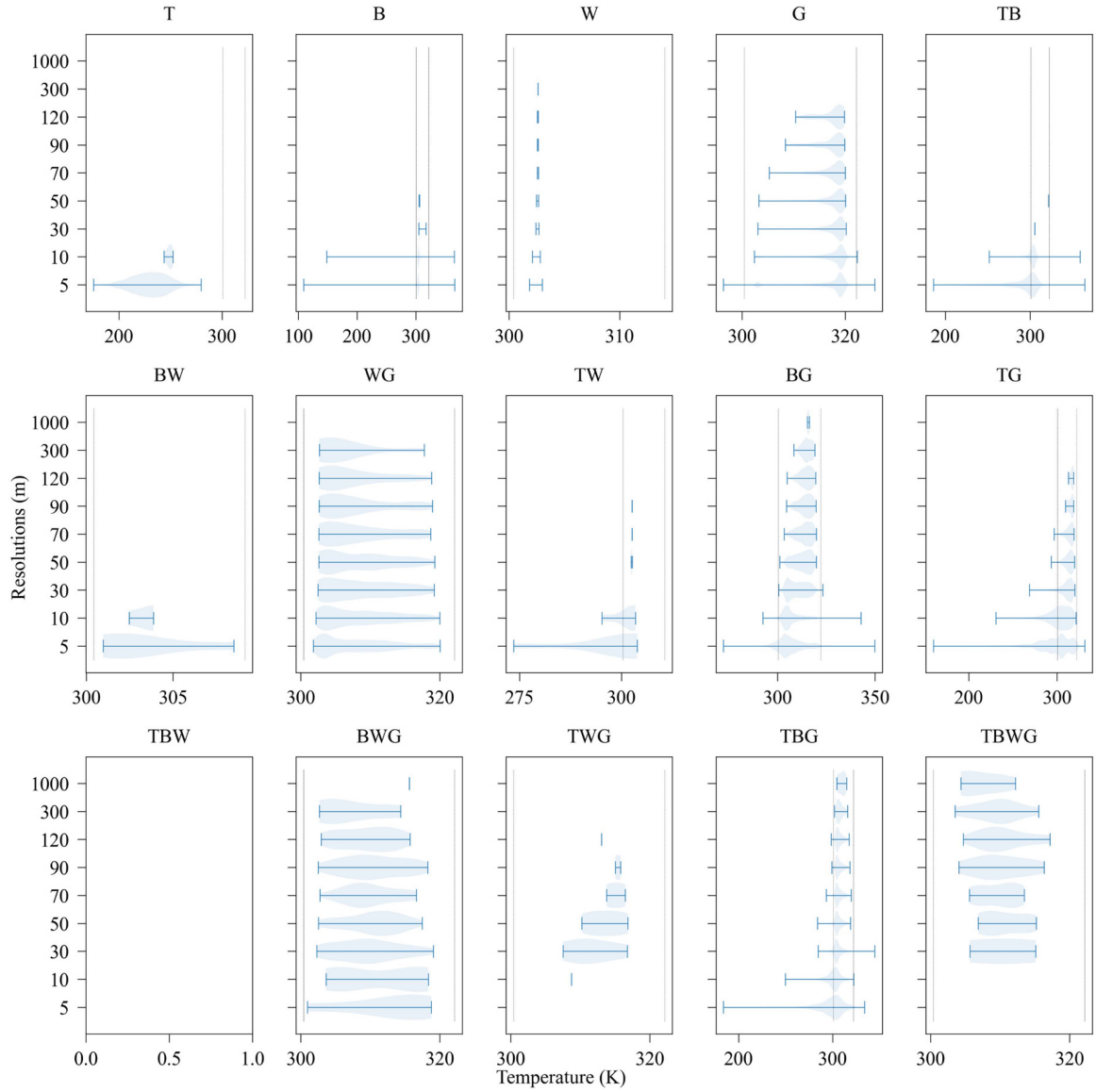

Fig. 10. TES retrieved pixelwise land surface temperature for Heraklion at nine spatial resolutions. The two vertical black dashed lines show the most tolerant acceptable boundary. (Because shadows can lead to changes in temperature, the acceptable boundaries are different even for the same pixel type. So here we drew the longest boundary of each type of pixel.) All subplots share the *y*-axis. See Fig. 4 for the meaning of the abbreviated titles of subplots. The spatial resolutions with no violin indicate no corresponding pixels type at that spatial resolution.

[72]. For example, the resolution is 1000 m for the moderate resolution imaging spectroradiometer (MODIS) and advanced very high-resolution radiometer (AVHRR), 300 m for HJ-1A/B, 120 m for the resolution of the Landsat thematic mapper (TM), 60 m for the enhanced thematic mapper plus (ETM+) and the ECOsystem Spaceborne Thermal Radiometer Experiment on Space Station, 100 m for the operational land imager/thermal infrared sensor, and 90 m for the advanced spaceborne thermal emission and reflection radiometer (ASTER). Even the future satellite mission micro satellite for thermal infrared ground surface imaging (MISTIGRI) only has a spatial resolution of 50 m. Therefore, when applied to urban satellite images, TES usually processes mixed rather than pure pixels. Airborne sensors, such as the MODIS/ASTER airborne simulator with 5–50 m spatial resolution depending on flight height and the hyperspectral thermal emission spectrometer (HyTES) with a resolution equal to 3.64 m at 2000-m flight altitude, can give enough pure pixels for urban studies. However, the use of airborne sensors is expensive and time consuming. Besides, airborne images cannot provide wide coverage and long observation period data like satellite images.

We evaluate the TES accuracy on both pure and mixed pixels. For both types of pixels, the increasing spatial resolution increases the value range of TES retrieved LST and LSE. The reason for this may be due to the increasing value range of pixel radiance because of the high heterogeneity (i.e., shadow and pixel nonplanarity) in the high-resolution images, and these phenomena are smoothed in the coarse resolution remote sensing

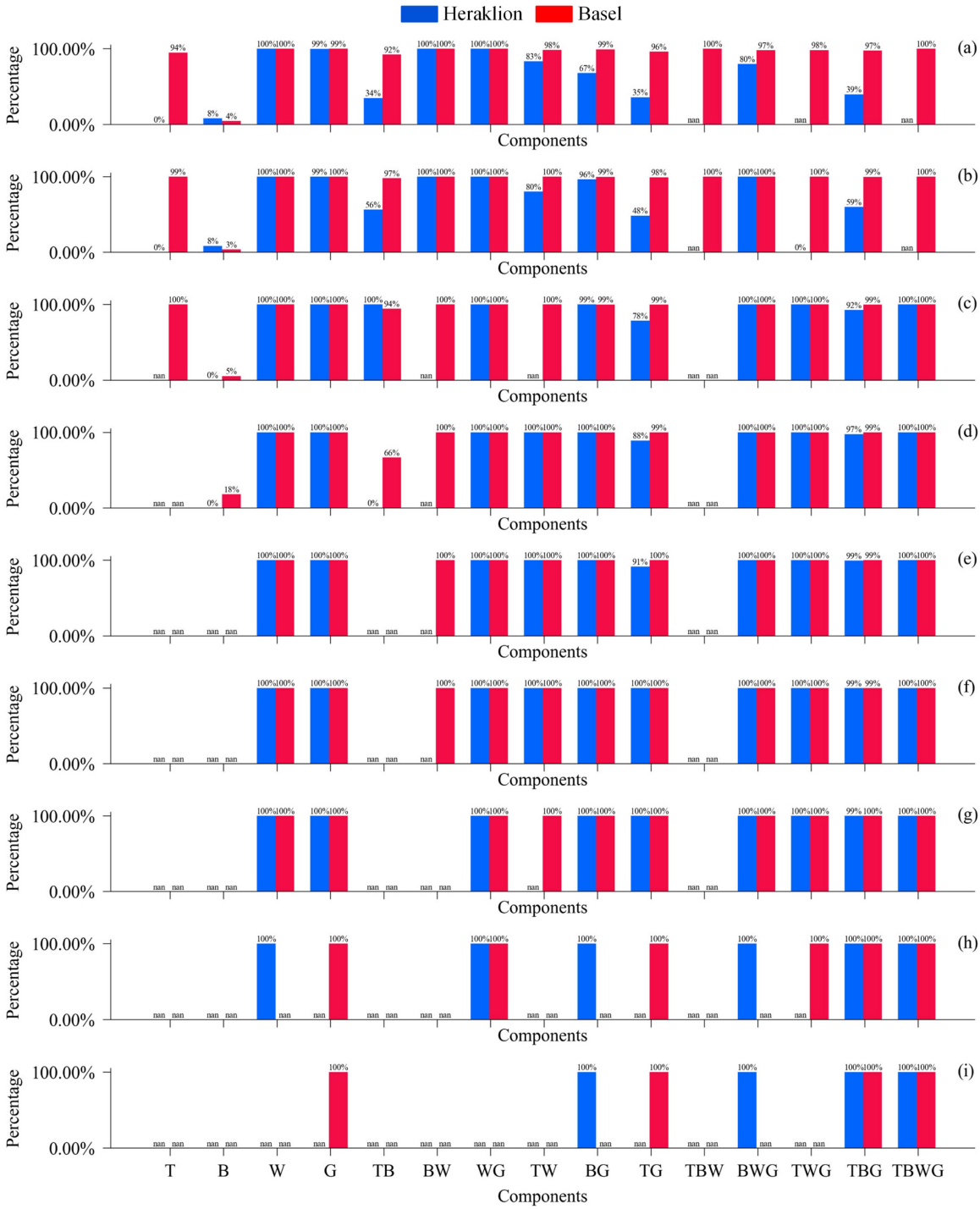

Fig. 11. Proportion of acceptable pixels $\mathcal{P}$ per pixel type at nine spatial resolutions: (a) 5 m, (b) 10 m, (c) 30 m, (d) 50 m, (e) 70 m, (f) 90 m, (g) 120 m, (h) 300 m, and (i) 1000 m. See Fig. 4 for the meaning of the letters on the horizontal axis. The difference between "0%" and "nan" is that "0%" means that there are no corresponding acceptable pixels, but there is a corresponding type of pixel, while "nan" means that the corresponding type of pixel does not exist.

images. However, even if the pixel is not a pure isothermal pixel, the average temperature and emissivity obtained by TES can remain in an acceptable range. It should note that a different acceptable boundary of the acceptable pixel may dramatically change our results.

The analysis of TES intermediate results stressed that problematic pixels occur mainly in three cases: 1) The iterative calculation of R_k shows a divergence in the NEM module; 2) The emissivity becomes too low, leading to negative R_k during the iterations in the NEM module; 3) The error produced from the MMD module.

Similar to other studies [26], buildings do not perform well. One possible reason may be due to the MMD module. The MMD coefficients ($a = 0.994$, $b = -0.687$, $c = 0.737$) may not work

well for manmade materials. In order to improve the ability of the TES algorithm to retrieve temperature and emissivity in cities, some studies [27] fit the coefficients of the MMD module only using manmade spectral library, which can overcome the low performance of TES algorithm in the manmade materials. However, because our land cover is not limited to the manmade land cover, and we want to get a general conclusion, we use the coefficients ($a = 0.994, b = -0.687, c = 0.737$) of ASTER in the original paper. For studies that focusing on manmade materials, fitting the MMD coefficients using only manmade materials is recommended.

Considering that authentic remote sensing images are much more complicated than simulated data (i.e., interclass spectral variability), we believe that the proportion of mixed pixels in the real case is much higher than the evaluation in this study, which undoubtedly poses a challenge to the algorithm based on the assumption of pure pixels. Therefore, our study stresses the importance of using methods that consider mixed (i.e., TRUST [22] or TRUST-DNS [23]) and nonflat pixel effects for LSE and LST estimation over urban areas with the current satellite image resolutions.

B. Conclusion

This article investigates the mixed pixel distribution in urban areas and evaluates the TES performance at several satellite spatial resolutions. Our approach is based on satellite radiance images simulated by the DART model at nine spatial resolutions. The main conclusions are summarized below as follows.

1) The 30-m spatial resolution appears to be a critical threshold for the proportion of pure pixels in urban satellite images. When the spatial resolution is below 30 m, the percentage of pure pixels increases slowly with increasing resolution; when the spatial resolution is above 30 m, the percentage of pure pixels increases rapidly with increasing resolution.
2) For the homogeneous, isothermal, flat, and shadow-free land cover, the accuracy of TES performs stably with the change of image spatial resolution. For the highly heterogeneous land cover, the accuracy of the TES method even decreases with the increase of spatial resolution. The reason may be that higher spatial resolution enhances spatial heterogeneity (due to shadow and pixel nonplanarity).
3) For mixed pixels, the average temperature and emissivity obtained by TES are basically in an acceptable range.

Our study considers nonisothermal and mixed urban pixels because current thermal infrared satellite sensors have a spatial resolution coarser than 50 m. Our results contribute to the selection and combination of endmembers in spectral mixing models and the assessment of the robustness of the TES method in urban studies. They can be extrapolated to other cities because Basel and Heraklion are representative of many European cities. Nevertheless, our study is obtained under a limited number of conditions, and the variations of these factors may affect our results, such as the change of observation angle, the selection of error pixel boundary values, etc. Further works must be done to extrapolate more conditions. Furthermore, the distribution of mixed pixels in actual satellite images is probably wider than in simulated images. It stresses the need for more detailed urban databases to bring the simulated pixel distribution closer to the actual situation.

ACKNOWLEDGMENT

The authors would like to thank DART team members Eric Chavanon, Dr. Nicolas Lauret, Jordan Guilleux at University of Toulouse for steady guidance on DART software. The authors also thank Lisai Cao, Dr. Jian Li, Dr. Peng Lu, Yinghui Ye, Zhuqiang Li at Jilin University for providing research instruments.

REFERENCES

[1] B. Cao et al., "A review of earth surface thermal radiation directionality observing and modeling: Historical development, current status and perspectives," *Remote Sens. Environ.,* vol. 232, 2019, Art. no. 111304.
[2] Z. Chen and Y. Zhang, "Quantitative identification of temporal-spatial variations of urban heat island (UHI) effects in Changchun, China," *IEEE J. Sel. Topics Appl. Earth Observ.,* vol. 15, pp. 3052–3060, 2022.
[3] D. Sun, C. Hu, Y. Wang, Z. Wang, and J. Zhang, "Examining spatio-temporal characteristics of urban heat islands and factors driving them in Hangzhou, China," *IEEE J. Sel. Topics Appl. Earth Observ.*, vol. 14, pp. 8316–8325, 2021.
[4] L. Li, Z. Zhao, H. Wang, L. Shen, N. Liu, and B.-J. He, "Variabilities of land surface temperature and frontal area index based on local climate zone," *IEEE J. Sel. Topics Appl. Earth Observ.,* vol. 15, pp. 2166–2174, 2022.
[5] W. Morrison et al., "Atmospheric and emissivity corrections for ground-based thermography using 3D radiative transfer modelling," *Remote Sens. Environ.,* vol. 237, 2020, Art. no. 111524.
[6] C. Ru et al., "Land surface temperature retrieval from landsat 8 thermal infrared data over urban areas considering geometry effect: Method and application," *IEEE Trans. Geosci. Remote Sens.,* vol. 60, 2022, Art. no. 5000716.
[7] M. A. Dissegna et al., "Modeling mean radiant temperature distribution in urban landscapes using DART," *Remote Sens,* vol. 13, no. 8, 2021, Art. no. 1443.
[8] H. Zeng, H. Ren, J. Nie, J. Zhu, X. Ye, and C. Jiang, "Land surface temperature and emissivity retrieval from nighttime middle and thermal infrared images of Chinese Fengyun-3D MERSI-II," *IEEE J. Sel. Topics Appl. Earth Observ.,* vol. 14, pp. 7724–7733, 2021.
[9] X. Zhang, J. Zhou, F.-M. Göttsche, W. Zhan, S. Liu, and R. Cao, "A method based on temporal component decomposition for estimating 1-km all-weather land surface temperature by merging satellite thermal infrared and passive microwave observations," *IEEE Trans. Geosci. Remote Sens.,* vol. 57, no. 7, pp. 4670–4691, Jul. 2019.
[10] Z. Meng, R. Zhao, Z. Cai, J. Ping, Z. Tang, and S. Chen, "Microwave thermal emission at tycho area and its geological significance," *IEEE J. Sel. Topics Appl. Earth Observ.,* vol. 10, no. 6, pp. 2984–2990, Jun. 2017.
[11] B. Cao et al., "Evaluation of four kernel-driven models in the thermal infrared band," *IEEE Trans. Geosci. Remote Sens.,* vol. 57, no. 8, pp. 5456–5475, Aug. 2019.
[12] J. Sobrino, C. Mattar, J. Gastellu-Etchegorry, J. Jimenez-Munoz, and E. Grau, "Evaluation of the DART 3D model in the thermal domain using satellite/airborne imagery and ground-based measurements," *Int. J. Remote Sens.,* vol. 32, no. 22, pp. 7453–7477, 2011.
[13] R. Paugam, M. J. Wooster, and G. Roberts, "Use of handheld thermal imager data for airborne mapping of fire radiative power and energy and flame front rate of spread," *IEEE Trans. Geosci. Remote Sens.,* vol. 51, no. 6, pp. 3385–3399, Jun. 2013.
[14] X. Zheng, Z. Li, F. Nerry, and X. Zhang, "A new thermal infrared channel configuration for accurate land surface temperature retrieval from satellite data," *Remote Sens. Environ.,* vol. 231, 2019, Art. no. 111216.
[15] S.-B. Duan, Z.-L. Li, and P. Leng, "A framework for the retrieval of all-weather land surface temperature at a high spatial resolution from polar-orbiting thermal infrared and passive microwave data," *Remote Sens. Environ.,* vol. 195, pp. 107–117, 2017.
[16] E. G. Njoku and D. Entekhabi, "Passive microwave remote sensing of soil moisture," *J. Hydrol.,* vol. 184, no. 1, pp. 101–129, 1996.

[17] C. Ottlé and D. Vidal-Madjar, "Estimation of land surface temperature with NOAA9 data," *Remote Sens. Environ.,* vol. 40, no. 1, pp. 27–41, 1992.

[18] L. M. McMillin, "Estimation of sea surface temperatures from two infrared window measurements with different absorption," *J. Geophys. Res.,* vol. 80, no. 36, pp. 5113–5117, 1975.

[19] J. Sobrino and M. Romaguera, "Land surface temperature retrieval from MSG1-SEVIRI data," *Remote Sens. Environ.,* vol. 92, no. 2, pp. 247–254, 2004.

[20] A. Gillespie, S. Rokugawa, T. Matsunaga, J. S. Cothern, S. Hook, and A. B. Kahle, "A temperature and emissivity separation algorithm for advanced spaceborne thermal emission and reflection radiometer (ASTER) images," *IEEE Trans. Geosci. Remote Sens.,* vol. 36, no. 4, pp. 1113–1126, Jul. 1998.

[21] M. Pivovarník, S. J. S. Khalsa, J. C. Jiménez-Muñoz, and F. Zemek, "Improved temperature and emissivity separation algorithm for multispectral and hyperspectral sensors," *IEEE Trans. Geosci. Remote Sens.,* vol. 55, no. 4, pp. 1944–1953, Apr. 2017.

[22] M. Cubero-Castan, J. Chanussot, V. Achard, X. Briottet, and M. Shimoni, "A physics-based unmixing method to estimate subpixel temperatures on mixed pixels," *IEEE Trans. Geosci. Remote Sens.,* vol. 53, no. 4, pp. 1894–1906, Apr. 2015.

[23] C. Granero-Belinchon, A. Michel, V. Achard, and X. Briottet, "Spectral unmixing for thermal infrared multi-spectral airborne imagery over urban environments: Day and night synergy," *Remote Sens.,* vol. 12, no. 11, 2020, Art. no. 1871.

[24] E. F. Collins, D. A. Roberts, and C. C. Borel, "Spectral mixture analysis of simulated thermal infrared spectrometry data: An initial temperature estimate bounded TESSMA search approach," *IEEE Trans. Geosci. Remote Sens.,* vol. 39, no. 7, pp. 1435–1446, Jul. 2001.

[25] F. Jacob et al., "A simulation-based error budget of the TES method for the design of the spectral configuration of the micro-bolometer-based MISTIGRI thermal infrared sensor," *IEEE Trans. Geosci. Remote Sens.,* vol. 60, 2022, Art. no. 5000919.

[26] V. Payan and A. Royer, "Analysis of temperature emissivity separation (TES) algorithm applicability and sensitivity," *Int. J. Remote Sens.,* vol. 25, no. 1, pp. 15–37, 2004.

[27] R. Oltra-Carrió, M. Cubero-Castan, X. Briottet, and J. A. Sobrino, "Analysis of the performance of the TES algorithm over urban areas," *IEEE Trans. Geosci. Remote Sens.,* vol. 52, no. 11, pp. 6989–6998, Nov. 2014.

[28] R. Welch, "Spatial resolution requirements for urban studies," *Int. J. Remote Sens.,* vol. 3, no. 2, pp. 139–146, 1982.

[29] J. P. Gastellu-Etchegorry et al., "Why to model remote sensing measurements in 3D? Recent advances in dart: Atmosphere, topography, large landscape, chlorophyll fluorescence and satellite image inversion," in *Proc. IEEE 5th Int. Conf. Adv. Technol. Signal Image Process.*, 2020, pp. 1–6.

[30] J.-P. Gastellu-Etchegorry, V. Demarez, V. Pinel, and F. Zagolski, "Modeling radiative transfer in heterogeneous 3-D vegetation canopies," *Remote Sens. Environ.,* vol. 58, no. 2, pp. 131–156, 1996.

[31] J.-P. Gastellu-Etchegorry, "3D Modeling of satellite spectral images, radiation budget and energy budget of urban landscapes," *Meteorol. Atmos. Phys.,* vol. 102, no. 3/4, pp. 187–207, 2008.

[32] J.-P. Gastellu-Etchegorry et al., "Discrete anisotropic radiative transfer (DART 5) for modeling airborne and satellite spectroradiometer and LIDAR acquisitions of natural and urban landscapes," *Remote Sens.,* vol. 7, no. 2, pp. 1667–1701, 2015.

[33] J.-P. Gastellu-Etchegorry et al., "DART: Recent advances in remote sensing data modeling with atmosphere, polarization, and chlorophyll fluorescence," *IEEE J. Sel. Topics Appl. Earth Observ.,* vol. 10, no. 6, pp. 2640–2649, Jun. 2017.

[34] T. Yin, J.-P. Gastellu-Etchegorry, N. Lauret, E. Grau, and J. Rubio, "A new approach of direction discretization and oversampling for 3D anisotropic radiative transfer modeling," *Remote Sens. Environ.,* vol. 135, pp. 213–223, 2013.

[35] T. Yin, J. Qi, B. D. Cook, D. C. Morton, S. Wei, and J.-P. Gastellu-Etchegorry, "Modeling small-footprint airborne Lidar-derived estimates of gap probability and leaf area index," *Remote Sens.,* vol. 12, no. 1, 2019, Art. no. 4.

[36] Z. Zhen et al., "Quantitative analysis of DART calibration accuracy for retrieving spectral signatures over urban area," *IEEE J. Sel. Topics Appl. Earth Observ.,* vol. 14, pp. 10057–10068, 2021.

[37] J.-P. Gastellu-Etchegorry et al., "Simulation of satellite, airborne and terrestrial LiDAR with DART (I): Waveform simulation with quasi-Monte Carlo ray tracing," *Remote Sens. Environ.,* vol. 184, pp. 418–435, 2016.

[38] T. Yin, N. Lauret, and J.-P. Gastellu-Etchegorry, "Simulation of satellite, airborne and terrestrial LiDAR with DART (II): ALS and TLS multi-pulse acquisitions, photon counting, and solar noise," *Remote Sens. Environ.,* vol. 184, pp. 454–468, 2016.

[39] J. Gastellu-Etchegorry et al., "Recent improvements in the dart model for atmosphere, topography, large landscape, chlorophyll fluorescence, satellite image inversion," in *Proc. IEEE Int. Geosci. Remote Sens. Symp.*, 2020, pp. 3455–3458.

[40] M. P. Ferreira et al., "Retrieving structural and chemical properties of individual tree crowns in a highly diverse tropical forest with 3D radiative transfer modeling and imaging spectroscopy," *Remote Sens. Environ.,* vol. 211, pp. 276–291, 2018.

[41] T. Miraglio, K. Adeline, M. Huesca, S. Ustin, and X. Briottet, "Joint use of PROSAIL and DART for fast LUT building: Application to gap fraction and leaf biochemistry estimations over sparse oak stands," *Remote Sens.,* vol. 12, no. 18, pp. 2925, 2020.

[42] Z. Zhen, "Simulation de la Réflectance de la Végétation et Inversion des Propriétés Bio-Optiques Basées Sur Un Modèle de Transfert Radiatif Tridimensionnel," Ph.D. dissertation, Centre d'Etudes Spatiales de la Biosphère, Université de Toulouse, Toulouse, France, 2021.

[43] Z. Zhen, S. Chen, W. Qin, J. Li, M. Mike, and B. Yang, "A modified transformed soil adjusted vegetation index for cropland in Jilin Province, China," *Acta Geol. Sinica-England Ed.*, vol. 93, no. S3, pp. 173–176, 2019.

[44] Z. Zhen et al., "Potentials and limits of vegetation indices with BRDF signatures for soil-noise resistance and estimation of leaf area index," *IEEE Trans. Geosci. Remote Sens.,* vol. 58, no. 7, pp. 5092–5108, Jul. 2020.

[45] Z. Zhen et al., "Using the negative soil adjustment factor of soil adjusted vegetation index (SAVI) to resist saturation effects and estimate leaf area index (LAI) in dense vegetation areas," *Sensors,* vol. 21, no. 6, 2021, Art. no. 2115.

[46] N. Chrysoulakis et al., "Urban energy exchanges monitoring from space," *Sci. Rep.,* vol. 8, no. 1, pp. 1–8, 2018.

[47] L. Landier, "Modélisation 3D Du Bilan Radiatif des Milieux Urbains Par Inversion D'images Satellites en Cartes de Réflectance et de Température des Matériaux Urbains," Ph.D. dissertation, Centre d'Etudes Spatiales de la Biosphère, Université de Toulouse, Toulouse, France, 2018.

[48] L. Landier et al., "Calibration of urban canopies albedo and 3D shortwave radiative budget using remote-sensing data and the DART model," *Eur. J. Remote Sens.,* vol. 51, no. 1, pp. 739–753, 2018.

[49] Z. Mitraka, N. Chrysoulakis, Y. Kamarianakis, P. Partsinevelos, and A. Tsouchlaraki, "Improving the estimation of urban surface emissivity based on sub-pixel classification of high resolution satellite imagery," *Remote Sens. Environ.,* vol. 117, pp. 125–134, 2012.

[50] L. Landier et al., "3D modeling of radiative transfer and energy balance in urban canopies combined to remote sensing acquisitions," in *Proc. IEEE Int. Geosci. Remote Sens. Symp.*, 2016, pp. 6738–6741.

[51] C. Feigenwinter et al., "Spatial distribution of sensible and latent heat flux in the city of Basel (Switzerland)," *IEEE J. Sel. Topics Appl. Earth Observ.,* vol. 11, no. 8, pp. 2717–2723, Aug. 2018.

[52] C. Feigenwinter et al., "Spatial distribution of sensible and latent heat flux in the URBANFLUXES case study city Basel (Switzerland)," in *Proc. Joint Urban Remote Sens. Event*, 2017, pp. 1–4.

[53] Y. Wang and J.-P. Gastellu-Etchegorry, "DART: Improvement of thermal infrared radiative transfer modelling for simulating top of atmosphere radiance," *Remote Sens. Environ.,* vol. 251, 2020, Art. no. 112082.

[54] G. E. Thomas and K. Stamnes, *Radiative Transfer in the Atmosphere and Ocean*. Cambridge, U.K.: Cambridge Univ. Press, 2002.

[55] ASTER. "ASTER spectral response function," [Online]. Available: https://asterweb.jpl.nasa.gov/content/01_mission/03_instrument/archive/tir.txt

[56] M. R. Behera, C. Chun, S. Palani, and P. Tkalich, "Temporal variability and climatology of hydrodynamic, water property and water quality parameters in the West Johor Strait of Singapore," *Mar. Pollut. Bull.,* vol. 77, no. 1/2, pp. 380–395, 2013.

[57] V. Realmuto, "Separating the effects of temperature and emissivity: Emissivity spectrum normalization," in *Proc. 2nd Thermal Infrared Multispectral Scanner Workshop, Jet Propulsion Lab.*, 1990, pp. 31–35.

[58] K. Watson, "Spectral ratio method for measuring emissivity," *Remote Sens. Environ.,* vol. 42, no. 2, pp. 113–116, 1992.

[59] T. Matsunaga, "A temperature-emissivity separation method using an empirical relationship between the mean, the maximum, and the minimum of the thermal infrared emissivity spectrum," *J. Remote Sens. Soc. Jpn.,* vol. 14, no. 3, pp. 230–241, 1994.

[60] S. J. Hook, *HyspIRI Level-2 Thermal Infrared (TIR) Land Surface Temperature and Emissivity Algorithm Theoretical Basis Document*. Pasadena, CA, USA: Jet Propulsion Laboratory, National Aeronautics and Space Administration, 2011.
[61] F. Becker and Z. L. Li, "Surface temperature and emissivity at various scales: Definition, measurement and related problems," *Remote Sens. Rev.,* vol. 12, no. 3/4, pp. 225–253, 1995.
[62] J. M. Norman and F. Becker, "Terminology in thermal infrared remote sensing of natural surfaces," *Agriculture Forest Meteorol.,* vol. 77, no. 3/4, pp. 153–166, 1995.
[63] J. Cheng, *Research on Temperature and Emissivity Separation Algorithm for Hyperspectral Infrared Data*. Beijing, China: Chinese Academy of Sciences, 2008.
[64] R. C. O. Carrió, *Thermal Remote Sensing of Urban Areas: The Case of Study of the Urban Heat Island of Madrid*. Facultat de Física, 2013.
[65] C. Coll et al., "Temperature and emissivity separation from ASTER data for low spectral contrast surfaces," *Remote Sens. Environ.,* vol. 110, no. 2, pp. 162–175, 2007.
[66] G. C. Hulley and S. J. Hook, "The North American ASTER land surface emissivity database (NAALSED) version 2.0," *Remote Sens. Environ.,* vol. 113, no. 9, pp. 1967–1975, 2009.
[67] A. R. Gillespie, E. A. Abbott, L. Gilson, G. Hulley, J.-C. Jiménez-Muñoz, and J. A. Sobrino, "Residual errors in ASTER temperature and emissivity standard products AST08 and AST05," *Remote Sens. Environ.,* vol. 115, no. 12, pp. 3681–3694, 2011.
[68] J. Franke, D. A. Roberts, K. Halligan, and G. Menz, "Hierarchical multiple endmember spectral mixture analysis (MESMA) of hyperspectral imagery for urban environments," *Remote Sens. Environ.,* vol. 113, no. 8, pp. 1712–1723, 2009.
[69] H. Zhang, Y. Qiu, L. Chen, and J. Zhao, "Analysis of urban reflectance and urban sprawl in China using TM/ETM+ imagery," in *Proc. Multispectral, Hyperspectral, Ultraspectral Remote Sens. Technol., Techn., Appl.*, 2006, pp. 318–324.
[70] J. Sobrino, R. Oltra-Carrió, G. Sòria, R. Bianchi, and M. Paganini, "Impact of spatial resolution and satellite overpass time on evaluation of the surface urban heat island effects," *Remote Sens. Environ.,* vol. 117, pp. 50–56, 2012.
[71] G. Meister, A. Rothkirch, H. Spitzer, and J. K. Bienlein, "Large-scale bidirectional reflectance model for urban areas," *IEEE Trans. Geosci. Remote Sens.,* vol. 39, no. 9, pp. 1927–1942, Sep. 2001.
[72] Q. Zhao and E. A. Wentz, "A MODIS/ASTER airborne simulator (MASTER) imagery for urban heat island research," *Data,* vol. 1, no. 1, 2016, Art. no. 7.

Zhijun Zhen received the Ph.D. degree in geographic information system from Jilin University, Changchun, China, in 2021, in collaboration with CESBIO, Toulouse III University, Toulouse, France.

He is currently a Lecturer with the College of Geoexploration Science and Technology, Jilin University. His research interests include radiative transfer modeling, retrieving, measuring, and analyzing surface bidirectional reflectance distribution function/albedo.

Shengbo Chen (Member, IEEE) received the Ph.D. degree in geo-exploration and information technology from the College of Geoexploration Science and Technology, Jilin University, Changchun, China, in 2000.

He is currently a Professor with the College of Geoexploration Science and Technology, Jilin University. He has authored or coauthored more than 200 papers. His research interests include quantitative remote sensing and lunar remote sensing.

Dr. Chen is a Member of the AGU.

Tiangang Yin received the Ph.D. degree in ocean, atmosphere, and continental surfaces from CESBIO, University of Toulouse, Toulouse, France, in 2015.

He has been extensively involved in the developments of the DART model for the past nine years, especially for LiDAR, atmosphere, and fluorescence modeling. He has been a Research Fellow with the Massachusetts Institute of Technology, Cambridge, MA, USA. He was part of the Research Faculty with the Earth System Science Interdisciplinary Center, Riverdale Park, MD, USA, the University of Maryland, College Park, MD, USA, and the NASA Goddard Space Flight Center, Greenbelt, MD, USA. He is currently working with the Department of Land Surveying and Geo-Informatics, the Hong Kong Polytechnic University, Hong Kong, China.

Jean-Philippe Gastellu-Etchegorry (Member, IEEE) received the B.Sc. degree in electricity from ENSEEIHT, Toulouse, France, in 1978, the aggregation degree in physics from Paris 6 University, Paris, France, in 1981, and the Ph.D. degrees in solar physics in 1983, and remote sensing in 1989, from Toulouse III University (UT3), France.

He worked with PUSPICS-Remote Sensing Center, Gadjah Mada University, Yogyakarta, Indonesia, and SEAMEO, Bangkok, Thailand, in 1984–90. Then, he joined the Remote Sensing Department with CESR, Toulouse, France, and CESBIO, Toulouse, France, in 1995. He is currently a Professor with UT3. He has been developing the DART model (https://dart.omp.eu) since 1993. His research interests include 3-D radiative transfer modeling.